ACS APPLIED MATERIALS & INTERFACES

Article

Aptamer-templated silver nanoclusters embedded in zirconium metal–organic framework for bifunctional electrochemical and SPR aptasensors toward carcinoembryonic antigen

Chuanpan Guo, Fangfang Su, Yingpan Song, Bin Hu, Minghua Wang, Linghao He, Donglai Peng, and Zhihong Zhang

ACS Appl. Mater. Interfaces, **Just Accepted Manuscript** • DOI: 10.1021/acsami.7b14952 • Publication Date (Web): 07 Nov 2017

Just Accepted

ACS Publications

ACS Applied Materials & Interfaces is published by the American Chemical Society.
1155 Sixteenth Street N.W., Washington, DC 20036

Aptamer-templated silver nanoclusters embedded in zirconium metal–organic framework for bifunctional electrochemical and SPR aptasensors toward carcinoembryonic antigen

Chuanpan Guo, Fangfang Su, Yingpan Song, Bin Hu, Minghua Wang, Linghao He, Donglai Peng, Zhihong Zhang*

Henan Provincial Key Laboratory of Surface and Interface Science, Zhengzhou University of Light Industry, Zhengzhou, 450001, P. R. China.

*Corresponding author:

Tel.: +86-37186609676

E-mail: mainzhh@163.com

ABSTRACT: This study reported a novel biosensor based on the nanocomposite of zirconium metal–organic framework (Zr-MOF, UiO-66) embedded with silver nanoclusters (Ag NCs) using the carcinoembryonic antigen (CEA)-targeted aptamer as template (AgNCs@Apt@UiO-66). The synthesized AgNCs@Apt@UiO-66 nanocomposite not only possesses good biocompatibility, active electrochemical performance, highly drug loading capacity, and strong bioaffinity, but also can be dispersed to form two-dimensional nanocomposite with nano-scale thickness. As such, the use of the AgNCs@CEA-aptamer enables sensitive and selective detection of trace CEA by the AgNC@Apt@UiO-66-based aptasensor, further concurrently being exploited as scaffold for surface plasmon resonance spectroscopy (SPR) and electrochemical biosensors. The results showed that the proposed electrochemical aptasensor exhibits high sensitivity with a low detection limit (LOD) of 8.88 and 4.93 $pg \cdot mL^{-1}$ deduced from electrochemical impedance spectroscopy and differential pulse voltammetry, respectively, within a broad linear range of the CEA concentration (0.01−10 $ng \cdot mL^{-1}$). Meanwhile, the developed SPR biosensor exhibited a slightly high LOD of 0.3 $ng \cdot mL^{-1}$ within the CEA concentration of 1.0−250 $ng \cdot mL^{-1}$. The developed aptasensor also displayed high selectivity, good reproducibility, stability, acceptable regenerability, and applicability in real human serum samples. These results proved that the proposed aptamer-targeted Zr-MOF nanocomposite can be utilized in multiple-functionally biosensing, further promoting the potential application of Zr-MOF-related nanomaterials in clinical diagnosis.

KEYWORDS: *Silver nanoclusters; Zirconium metal–organic framework;*

Electrochemical aptasensor; Surface plasmon resonance; carcinoembryonic antigen

■INTRODUCTION

As a tumor marker, carcinoembryonic antigen (CEA) is a ~200 kDa glycoprotein in the immunoglobulin super family, and it plays an important role in the diagnosis and screening of many cancers.[1] Normally, the CEA content in biological samples of healthy human is lower than 5 $ng \cdot mL^{-1}$. High serum CEA level indicates the presence of cancer cells. Consequently, the sensitive and early determination of CEA is essential in prognosis of the original carcinoma and clinical tumor diagnoses. To date, many techniques, including enzyme-linked immunosorbent assay,[2] square wave voltammetry,[3] differential pulse voltammetry,[4] fluorescence,[5] capillary electrophoresis-chemiluminescence,[6] and electrochemiluminescence,[7] have been exploited for the trace determination of CEA. In comparison with conventional techniques, which often require highly expensive and complex equipment, skilled operators, and considerable amount of time for sample pretreatment,[1] electrochemical methods exhibit the advantages of simple instrumentation, high sensitivity, low cost, specific recognition, and fast response when applied to detect CEA.[8]

Additionally, based on the ability to measure the changes in the refractive index of the metal surface and the molecular interaction,[9] surface plasmon resonance spectroscopy (SPR) spectroscopy has been widely applied in numerous fields, such as clinical diagnosis, drug screening, environmental monitoring, and food safety, due to its advantages, including less time consumption, non-labeling, high sensitivity, and

high efficiency.[10,11] SPR is a remarkably suitable approach for measuring dissociation constants of drug–protein interactions because it covers a broad range of dissociation constants that are accessible (KD of $10^{-3.5}$–$10^{-10.5}$ M).[12] For instance, Ab-AuNPs can enhance SPR sensor response by three orders of magnitude and to detect CEA at concentrations as low as 12 pg·mL^{-1} (60 fM) in buffer and 40 pg·mL^{-1} (200 fM) in 50% blood plasma, which is currently the most sensitive AuNP-enhanced SPR biosensor for detection of CEA.[13]

Aptamers are nucleic acids (DNAs or RNAs) that evolved to specifically bound proteins or low-molecular-weight inorganic or organic substrates.[14] Given their specificity and high binding constants,[15,16] aptamers are used in assembly with nanomaterials and detection of heavy metals,[17] proteins,[18] and cancer cells.[19] Currently, aptamers that can specifically bind with CEA have been widely used for fabricating novel electrochemical biosensors.[20] Complex fabrication of electrode materials is often used to enhance the sensitivity of aptasensors. Actually, aptamer strands were often employed as template when preparing the silver nanoclusters (Ag NCs) [21] in order to reduce the tendency of Ag NCs to aggregate into large nanoparticles (NPs).[22] As known, Ag NPs exhibit unprecedented metallic properties with the emergence of SPR.[23] For instance, Ag NP probes-based localized surface plasmon resonance (LSPR) sensor has been investigated and characterized to demonstrate the selectivity of the sensor towards specific volatile liquid.[24] Except that the red shift in the SPR band of Ag NCs can be compared to SPR of a single Ag-NP, the DNA-templated Ag NCs also displays the strong interplasmonic interaction.[25]

Recently, metal–organic frameworks (MOFs), a class of porous materials assembled from metal/metal clusters and organic ligands, have been investigated extensively due to their high surface areas, well-defined porosities, and chemical tunability.[26,27] MOFs show promising applications in gas-separation and storage,[28] drug delivery,[29] sensing,[30] and catalysis.[31] Moreover, owing to the excellent adsorption characteristics and various grafting groups (e.g., $-NH_2$ or −COOH), porous MOFs are considered as ideal candidates that may facilitate the co-immobilization of metal ions and biological ligands.[32] Therefore, a series of new biosensors based on MOFs have been developed for detecting multiple antibiotics,[33] phosphoprotein,[34] HIV-1 ds-DNA sequences,[35] and so on. For instance, zeolitic imidazolate framework-8 (ZIF-8) with a combination of mesoporous and microporous channels immobilized with cytochrome c (Cyt c) was employed to selectively determine H_2O_2,[36] whereas Al-MOF-based electrochemical biosensor demonstrated high sensitivity with low detection limits of 0.70 and 0.40 pg mL^{-1} toward vomitoxin and salbutamol, respectively.[37] Among many MOFs, Zr-based MOFs exhibit great potential in practical applications due to their excellent water stability and low-cost production in large scale.[38] Owning to the strong bioaffinity and the high binding interaction of Zr−O−P between MOF frameworks and the DNA strands,[39] a series of Zr-MOF-based biosensors were fabricated to sensitively determine the analytes.[40,41] Especially, UiO-66 was selected as a template material since they are well-known for their optimal surface areas, along with an independent linker, and exceptional stability. Nevertheless, electrochemical measurements often provide the final adsorption results

of the target molecules, but not the adsorption kinetics. As mentioned above, this disadvantage of electrochemical method can be overcome by SPR. The position of the strong minimum that occurs at the SPR resonance condition depends sensitively on the refractive index of the material above and the thickness of the layer near the gold surface (<200 nm).[42] However, few work investigated the MOF-based SPR sensor due to the large size of MOF particles. In our previous work,[43] 2D Zr-MOF nanosheets with the thickness of 6.5−7.5 nm are used as the scaffold layer for the aptamer strand immobilization and the detection of mucin 1. The adsorption behaviors between electrochemical technique and SPR results show considerably close consistency.

Additionally, MOFs possess a degree of synthetic flexibility unmatched by those of other nanoscale templates, thereby allowing the systematical tailoring of pore shape, size, and chemistry.[27] For example, atom-precise Au and AuAg NCs with high purity are synthesized using MOFs as size-selection templates and by in situ reduction method.[44] However, the investigation of MOFs embedded with metal NCs is mainly focused on catalytic application. To date, only few studies reported about the application of the nanocomposite based on MOFs and NCs in the biosensing field. For instance, in order to amplify the LSPR response, a universal LSPR response amplification strategy based on the biomineralization of a MOF on the captured analyte proteins was fabricated, giving the differential ability of abiotic recognition elements and entrapment biomolecules to induce biomineralization of a MOF.[45] So far, there is no report about the multiple-functional development of MOFs on their

bifunctional applications on the electrochemical and SPR biosensing.

Inspired by the entrapping of NCs in MOFs and preparation of NCs using DNA or aptamer as template, we proposed a new strategy for the synthesis of a novel nanocomposite comprising of Ag NCs and Zr-MOFs (AgNCs@Apt@UiO-66, **Figure 1**). In the present study, AgNCs@Apt@UiO-66 was utilized considering its advantages: i) strong bioaffinity, water stability, and high specific surface area of UiO-66, ii) high electrochemical activity, strong SPR response, and acceptable fluorescence performance of Ag NCs, and iii) specific binding with CEA caused by the probe aptamer strands. Therefore, SPR and electrochemical techniques were combined to investigate the detection kinetics, and exhibited similar results for detecting CEA using the developed aptasensor based on the AgNCs@Apt@UiO-66 nanocomposite.

■EXPERIMENTAL SECTION

Synthesis of UiO-66 and AgNCs@Apt@UiO-66 nanocomposites. UiO-66 was synthesized by hydrothermal method according to literature.[38] In detail, 0.7 g of zirconium chloride ($ZrCl_4$) and 0.5 g of benzene-1,4-dicarboxylic acid (H_2BDC) were dissolved in 30 mL of N,N-dimethylformamide (DMF) at room temperature to form a homogeneous solution. Subsequently, 4.0 mL of trifluoroacetic acid and 3.5 mL of hydrochloric acid were added in the mixture solution and heated at 120 °C for 24 h. After cooling to room temperature in air, the resulting solid was isolated by centrifugation at 10,000 rpm and washed with DMF and methanol at least six times to remove the unreacted chemicals. The product was dried at 60 ℃ for 24 h in vacuum,

and the UiO-66 crystal was obtained.

Afterward, UiO-66 (1.0 mg) was dispersed in 1.0 mL of ultrapure water through ultrasonication for 0.5 h. Subsequently, 100 μL of $AgNO_3$ solution (0.1 mg·mL^{-1}) and 500 μL of CEA aptamer (1.0 μM) in phosphate buffer solution (PBS, pH 7.4) were added to the above-mentioned solution with vigorous stirring at room temperature for 5 min. The mixture was kept in dark at 4 °C. After 3 h, freshly prepared ice-cold $NaBH_4$ (100 μL, 2.3 mg·mL^{-1}) was added in the mixture with vigorous shaking and incubated at 4 °C for overnight. Finally, the AgNCs@Apt@UiO-66 nanocomposite was obtained.

Fabrication of AgNCs@Apt@UiO-66-based aptasensor. The UiO-66 and AgNCs@Apt@UiO-66 samples were dispersed into deionized water with a concentration of 1 mg·mL^{-1}. For fabrication of the electrochemical aptasensors based on UiO-66 and AgNCs@Apt@UiO-66, 5.0 μL of dispersion was dropped onto the Au electrode (AE) and SPR chip surface, separately. After drying in air, the modified AE was immersed in CEA solutions with different concentrations for 3 h to detect target CEA. The modified AE washed with PBS to remove the unattached CEA for next concentration measurement. The thickness of the AgNCs@Apt@UiO-66 nanofilm coated onto the SPR chip was determined by the KLA-Tencor Step Profiler.

Characterizations. X-ray photoelectron spectroscopy (XPS) analysis was determined using an AXIS HIS 165 spectrometer (Kratos Analytical, Manchester, UK) with a monochromatized Al K_α X-ray source (1486.71 eV photons). X-ray diffraction measurements (XRD) were recorded on a Rigaku D/Max-2500 X-ray diffractometer

using Cu K_α radiation. Chemical components were analyzed via Fourier transform infrared spectroscopy (FT-IR) by using a Bruker TENSOR27 spectrometer (32 scans at 4 cm^{-1} resolution). Solid state luminescent spectra were obtained on a Varian Cary Eclipse fluorescence spectrophotometer. UV-vis spectra were obtained through a computer-controlled UV-vis spectrometer (TU-1201, Beijing Instrument Company). The surface morphology of the synthesized samples was investigated through JSM-6490LV scanning electron microscope (SEM, Japan) and JEOL JEM-2100 high-resolution transmission electron microscopy (HR-TEM) with a field emission gun of 200 kV. Cell was quantified by measuring the absorbance at wavelength of 490 and 620 nm, using a microplate reader (Thermo Fisher Scientific, Inc., USA). Cellular uptake and intracellular distribution of materials was studied using a confocal laser scanning microscopy (CLSM LSM710, ZEISS, Germany).

Electrochemical measurements. All electrochemical measurements were conducted on a CHI 760E electrochemical working station (CH Instruments, Inc. Shanghai, China) with a conventional three-electrode system: the modified AE with the nanomaterials as the working electrode, a Pt wire as counter electrode, and an Ag/AgCl (saturated KCl) electrode as reference electrode. The electrochemical behaviors of the modified AE were evaluated through cyclic voltammetry (CV), electrochemical impedance spectroscopy (EIS), and differential pulse voltammetry (DPV) in 5 mM $K_3[Fe(CN)_6]/K_4[Fe(CN)_6]$ (1:1) and 0.1 M PBS. The scan range of CV was from −0.2 V to 0.8 V with a scan rate of 100 $mV \cdot s^{-1}$. EIS plots were recorded at a bias potential of 0.22 V *vs.* Ag/AgCl (saturated KCl) and 5 mV amplitude in the

frequency ranging from 0.01 Hz to 100 kHz. EIS spectra were analyzed using Zview2 software, of which EIS spectra were simulated using an equivalent circuit, consisted of solution resistance (R_s), charge-transfer resistance (R_{ct}), constant-phase element (CPE), and Warburg impedance (W_o).[46] DPV measurements were performed with the following parameters: impulse amplitude 50 mV, potential scan from −0.2 to 0.6 V, and step potential of 4 mV.

SPR measurements. SPR measurement was carried out using a Biacore™ X100 device (GE-Healthcare Bio-Sciences AB, Sweden) at 25 °C in PBS (pH 7.4). The equilibration baseline was accomplished in a continuous flow (5 μL·min^{-1}) of PBS through the SPR chip (SIA Kit Au) for 6 h. The concentration titration experiments were performed in PBS running buffer at predetermined concentrations (1, 4, 5, 10, 50, 100, and 250 ng·mL^{-1}) at a flow rate of 5 μL·min^{-1}. Ascorbic acid (AA), mucin 1 (MUC1), thrombin, mouse immunoglobulin G (IgG), and their mixture were used for specificity analysis of the SPR aptasensors at a flow rate of 5 μL·min^{-1}. After each measurement, the sensing surface was readily regenerated through consecutive injection of 1.0 M NaOH solution at a flow rate of 5 μL·min^{-1} for 4 min. The loading amount of the biomolecules on the SPR chip was evaluated by considering one resonance unit (*RU*) corresponding to a change in refractive of 10^{-6} and approximately 1 pg·mm^{-2} of bound protein.[47] And the sample channel size is 2.5(l) × 0.50(w) × 0.04(h) mm with a total surface area of 1.25 mm^2.

■RESULTS AND DISCUSSION

Sensor design. AgNCs@Apt@UiO-66 nanocomposite was prepared and used to

construct the electrochemical and SPR aptasensor for trace detection of CEA. For this novel nanocomposite, the CEA target aptamer was used as the template to synthesize Ag NCs. The resultant AgNCs@Apt was further embedded in the UiO-66 framework. Therefore, the aptamer strands can bind on the nanocomposite surface and penetrate into the nanocomposite interior. As such, the as-prepared nanocomposite integrated the individual advantage of each component, including biocompatibility, low toxicity, and good electrochemical activity of Ag NCs; high specific surface area, strong bioaffinity, and water stability of the Zr-MOF framework, and specificity of aptamers toward the target analytes. When detecting CEA, CEA aptamer would specifically bind and generate recognized binding interactions with CEA,[48] which further results in considerably low access of redox probe to the surface of modified AE and the decrease in electrochemical response. Moreover, this biorecognition between CEA and the aptamer strands, i.e., the CEA binding with sensitive layer, can deduce the change in a dielectric constant of the thin adjacent layer and increase its thickness, thereby leading to the variation in the corresponding resonance reflectivity of SPR.[40] Therefore, the combination of electrochemical techniques and SPR can provide comprehensive understanding of CEA detection based on this novel AgNCs@Apt@UiO-66-based aptasensor.

Chemical structure and component of AgNCs@Apt@UiO-66. FT-IR, XRD, UV-vis, and fluorescence spectra of the UiO-66 and AgNCs@Apt@UiO-66 nanocomposite are shown in **Figure S1** and discussed in **S2**. AgNCs@Apt@UiO-66 nanocomposite exhibited similar chemical structure to that of UiO-66 and high

fluorescence intensity. This nanocomposite can be further used as the scaffold for the biosensor. In addition, XPS was utilized as a powerful tool to determine the elemental composition and chemical status of the samples. The complete XPS survey spectra of UiO-66, AgNCs@Apt@UiO-66, and CEA/AgNCs@Apt@UiO-66 are shown in **Figure S2**, and the atomic% of each element is summarized in **Table S1**. To evaluate the chemical environment of each element in the nanocomposite, the high-resolution XPS spectra for all elements were deconvoluted according to the XPS Peakfit software. The C 1*s*, N 1*s*, and Zr 3*d* core-level XPS spectra of UiO-66, AgNCs@Apt@UiO-66, and CEA/AgNCs@Apt@UiO-66 are shown in **Figure S3**, and the detailed discussions are provided in **S2**. Furthermore, the P 2*p* and Ag 3*d* core-level XPS spectra of AgNCs@Apt@UiO-66 are illustrated in **Figure 2a**. The high-resolution P 2*p* spectrum was deconvoluted into two peaks with binding energies of 133.5 and 134.5 eV, which correspond to P $2p_{3/2}$ and P $2p_{1/2}$, respectively.[49] The high-resolution Ag 3*d* spectrum was separated into two peaks at 367.28 and 373.27 eV. This result implied the presence of Ag^0,[50] indicating the formation of Ag NCs. These results further proved that the AgNCs@Apt@UiO-66 was successfully prepared through this facile method under mild conditions. When the AgNCs@Apt@UiO-66 was used to detect CEA, the binding energies of P 2*p* and Ag 3*d* of CEA/AgNCs@Apt@UiO-66 (**Figure 2b**) showed no change, which suggested that the AgNCs@Apt@UiO-66 retained its original structure. The elemental analysis proved the successful fabrication of the AgNCs@Apt@UiO-66-based aptasensor for

detecting the targeted CEA, suggesting that this aptasensor can be used in the fields of biosensing or diagnostic analysis.

Surface morphology of AgNCs@Apt@UiO-66. FE-SEM and TEM were performed to study the surface performance and microstructure of UiO-66 and AgNCs@Apt@UiO-66. FE-SEM images (**Figure S5a** and **S5b**) demonstrated that the UiO-66 exhibits as cubic intergrown particles with size of 200−400 nm, and the particles were indeed a three-dimensional structure and form uniform distribution. TEM images **(Figure S5c** and **S5d**) depicted that many pores are present among the UiO-66 particles, which would benefit the Ag NCs and aptamer strands to further embed into the framework of UiO-66 to form homogeneous nanocomposite. According to the SEM images of AgNCs@Apt@UiO-66 (**Figure 3a** and **3b**), the UiO-66 retains its uniform distribution and porous structure. Additionally, the nanocomposite surface is rough, which indicated the existence of Ag NCs. As illustrated in TEM **(Figure 3c** and **3d**), most of the Ag NCs are evenly distributed as sphere-like structure with the average size of 4−5 nm. Ag NCs are also embedded uniformly onto the surface and into the interior of UiO-66. This result suggested that the aptamer strands were also present in UiO-66, which would lead to large amounts of CEA molecules to bind with the nanocomposite when detecting CEA. The lattice space of synthesized Ag NCs calculated from HR-TEM image was 0.204 nm, which corresponds to the (200) lattice plane of face-centered cubic structure of Ag. The concentric diffraction rings in selected area electron diffraction (SAED, the inset of **Figure 3d**) revealed the polycrystalline nature of AgNCs@Apt@UiO-66. The spots

could correspond to the reflections from the (200) and (111) lattice planes, as shown in **Figure 3d**. All the lattice planes support the unit cell structure of Ag.[51]

Biosensing performance of UiO-66 and AgNCs@Apt@UiO-66 for detecting CEA.

In this work, electrochemical techniques and SPR method were applied to investigate the biosensing performance of the as-developed UiO-66- and AgNCs@Apt@UiO-66-based aptasensors, including the sensitivity, selectivity, stability, reproducibility, and regenerability. First, electrochemical techniques, such as CV, EIS, and DPV, were applied to investigate the electrochemical responses of the material-modified electrodes, monitor both the construction and sensing process of the aptasensors, and provide significant information about all fabrication steps of the working electrode. Detailed CV discussions about the aptasensors are shown in **S4** and **Figure S6**. To further probe the electrochemical behaviors sensitively and efficiently, EIS was utilized to determine the CEA detection using the developed aptasensors based on AgNCs@Apt@UiO-66 and UiO-66 (**Figure 4a** and **4b**). The bare AE displayed small well-defined semicircle at high frequencies with R_{ct} value of 90.0 and 112.7 Ω for AgNCs@Apt@UiO-66 and UiO-66, respectively. After the modification with the nanocomposites, the impedance curve of AgNCs@Apt@UiO-66/AE consisted of large semicircle with significantly high R_{ct} value of 887 Ω. For the aptasensor modified with UiO-66, the electrode of the UiO-66/AE and Apt/UiO-66/AE exhibited the R_{ct} values of 1.61 and 1.75 kΩ. This result indicated that the AgNCs@Apt@UiO-66 and UiO-66 nanocomposites can increase the R_{ct} at the interface between the analyte solution and the electrodes, which

was attributed to the repulsion interaction between the negatively charged phosphate groups contained in the aptamer strands and the redox couple of $[Fe(CN)_6]^{3-/4-}$.[52] Furthermore, the AgNCs@Apt@UiO-66 and UiO-66 possessed porous structure, high specific area, and large amount of aptamer strands present in the nanocomposites, and all these factors further decreased the charge transfer at the interface between the electrolyte solution and the modified electrode. When detecting CEA using the two developed aptasensors, the semicircle of EIS curves further increased. The corresponding R_{ct} values of the semicircle curves were 1.23 and 1.94 kΩ. In the presence of CEA, the CEA-targeted aptamer strands specifically bound and reacted with CEA. Considering the insulation performance, the charge transfer at the interface was further hindered. Additionally, the difference in the R_{ct} values caused by the modified AE before and after the CEA detection can represent the binding amount of the CEA. Evidently, the ΔR_{ct} of the CEA binding on AgNCs@Apt@UiO-66-modified AE was approximately 337 Ω and that of the Apt@UiO-66-modified AE was considerably lower (192 Ω). This result suggested that the presence of the Ag NCs in AgNCs@Apt@UiO-66 was favorable to the detection of CEA, which can be attributed to the biocompatibility and good electrochemical activity of Ag NCs, the intrinsically high specific surface area of the UiO-66 framework, and the specific binding and reaction between aptamer strands and CEA. This enhanced CEA binding in different modified AEs was also investigated by SPR, which can provide the detailed binding kinetics of the CEA. As for the conventional biosensors, several steps are needed for their fabrication, i.e., the sensitive layer modified onto the electrode or

chips, the immobilization of probe, and the detection of the analytes. Once the first probe layer is adsorbed onto the sensitive layer surface, the further adsorption of other probe strands becomes very difficult owning to the electrostatic repulsion interaction between their negatively-charged phosphate groups ionized in the aqueous solution.[53,54] As a result, the detection efficiency of this kind of aptasensor toward the analytes is limited by the certain amount of the adsorbed probe. In case of the as-developed AgNCs@Apt@UiO-66 nanocomposite, the aptamer strands not only can promote the stability of the Ag NCs but also can lead to the combination of the Ag NCs with UiO-66 via the complex interaction, including the covalent bonds of P−O between the aptamer strands and UiO-66[55,56] and the interaction between special functional groups on the organic linkers of MOFs and negatively charged nucleic acid sequences.[43] Additionally, thanks to the combination of the UiO-66 with AgNCs@Apt, some defects existed in the interior of the MOF framework. This special nanosized scale would result in the penetration of the analytes into the nanocomposite interior. Consequently, the analytes can bind with the probe molecules both on the surface and in the interior,[40] further leading to the high detection efficiency of the AgNCs@Apt@UiO-66-based aptasensor.

Additionally, the same electrochemical characterizations for the CEA detection were performed using the developed aptasensor based on AgNCs@Apt@UiO-66 and UiO-66 nanocomposites by DPV, as shown in **Figures. 4c** and **4d**, respectively. The similar trend in the peak current value (I_p) during aptasensor fabrication and the CEA detection was observed. The I_p value was −56.33, −36.95, and −30.33 μA for bare AE,

AgNCs@Apt@UiO-66/AE, and CEA/AgNCs@Apt@UiO-66/AE and −55.97, −27.1, −23.44, and −19.05 μA for bare AE, UiO-66/AE, Apt/UiO-66/AE, and CEA/Apt@UiO-66/AE, respectively; these values indicated that the electrochemical activity decreased when the AE was successively modified with AgNCs@Apt@UiO-66 or UiO-66 and the binding of CEA. In addition, the difference in the peak current originating from the different modified AE was calculated. Result demonstrated no substantial change between the ΔI values, that is, 6.62 and 4.39 μA, which were attributed to the CEA adsorption on the AgNCs@Apt@UiO-66- and UiO-66-based aptasensors, respectively. Moreover, as supplied in **S4**, the similar results were obtained using CV technique, which were consistent with those originated from EIS and DPV.

The CEA was determined by the Apt/UiO-66 and AgNCs@Apt@UiO-66 nanocomposite with the thickness of 80±5 nm. As for the UiO-66 layer, the CEA detection procedure was carried out after the aptamer immobilization, which was also recorded by SPR (**Figure S8**). According to the relationship between the RU variation and the binding amount, the amount of immobilized aptamers on the UiO-66 was calculated to be 0.634 ng, which was much less than that of the AgNCs@Apt@UiO-66 nanocomposite, i.e., 13.01 ng. When the two nanomaterial films reached equilibrium in PBS, the CEA solution (10 ng·mL^{-1}) was introduced into the SPR flow cell, and the SPR reflective intensity of the interface was monitored using SPR for 2500 s (**Figure 4e**). For these two studied samples, the biorecognition between CEA molecules and the aptamer strands, i.e., protein adsorption onto the

biosensing matrix, reached equilibrium at 1080 s after injecting the CEA into the cell. After this stabilization period, the samples were rinsed with excess PBS, which resulted in the loss of some unbound protein molecules from the matrix surface. Apparently, the difference in *RU* before and after the CEA adsorption (ΔRU) for the AgNCs@Apt@UiO-66 was 710 *RU*, which was substantially higher than that for Apt/UiO-66 nanocomposite (approximately 62 *RU*). As mentioned previously, the embedded amount of the aptamer strands in the AgNCs@Apt@UiO-66 was much higher than that was adsorbed on UiO-66, thus leading to more CEA molecules to bind. This result also indicated that more CEA molecules were bound with the AgNCs@Apt@UiO-66 due to the high bioaffinity of Ag NCs and high content of the aptamer strands contained in the nanocomposite.

Sensitivity of the developed aptasensor based on AgNCs@Apt@UiO-66. To evaluate the analytical performance of the developed aptasensor, the AgNCs@Apt@UiO-66/AE was incubated with different concentrations of CEA and subsequently measured by EIS and DPV in $[Fe(CN)_6]^{3-/4-}$ and 0.1 M PBS. **Figure 5a** shows the Nyquist plots of AgNCs@Apt@UiO-66/AE for detecting different concentrations of CEA. The R_{ct} values gradually increased with increasing CEA concentrations over the range of 0.01−10.0 ng·mL^{-1} because of the efficient recognition of the CEA by the aptasensor. This increase may be due to considerable specific binding and reaction between CEA and the aptamer strands with an increasing CEA concentration at the modified electrode surface. Consequently, the R_{ct} value increased. When the ΔR_{ct} value ($\Delta R_{ct} = R_{ct,\,\mathrm{CEA}} - R_{ct,\,\mathrm{material}}$) of the developed

aptasensor before and after the CEA detection was referred as the determined signal (**Figure 5b**), the ΔR_{ct} was well proportional to the logarithm value of the CEA concentration (log C_{CEA}). The linear regression equation was ΔR_{ct} (kΩ) = 1.254 + 0.465 log C_{CEA} (ng·mL^{-1}), with the correlation coefficient (R^2) of 0.991. According to the Langmuir adsorption equation, the limit of detection (LOD) was low (8.88 pg·mL^{-1}, 0.56 pM) at a signal-to-noise (*s/n*) ratio of 3.

Similarly, DPV (**Figure 5c** and **5d**) was also used to investigate the analytical performance of the developed AgNCs@Apt@UiO-66/AE aptasensor. The CEA solutions at various concentrations were subsequently incubated into the electrochemical measurement system. The equation of ΔI_p (μA) = 21.05 + 6.08 log C_{CEA} (ng·mL^{-1}) with R^2 of 0.990 was obtained. The LOD was 4.93 pg·mL^{-1} (0.31 pM) at a *s/n* ratio of 3. **Table 1** suggests that the fabricated aptasensor is an excellent candidate for the ultrasensitive and rapid detection of CEA.

The sensitivity of the fabricated SPR biosensor based on the AgNCs@Apt@UiO-66 was investigated using the CEA solutions with different concentrations. As shown in **Figure 5e**, the *RU* intensity increased when the CEA concentration increased from 4.0 ng·mL^{-1} to 250 ng·mL^{-1}. This result indicated that the amount of CEA adsorbed on the SPR chip is highly dependent on its concentration, further confirming the specific binding and reaction between the aptamer strands and CEA. Taking the SPR *RU* variation as a function of the CEA concentration **(Figure 5f),** a good linear correlation with the CEA concentration was observed. The equation of *RU* = 1071 log C_{CEA} − 424.13 (ng·mL^{-1}) with R^2 of 0.993 was simulated within the

CEA concentration range of 4.0−250 ng·mL^{-1} with a LOD of 0.3 ng·mL^{-1} under the optimal conditions. It is clear that the LOD derived from SPR was higher than those calculated from the electrochemical technique. This difference was possibly due to the insensitivity of the SPR instrument. Nevertheless, the fabricated SPR biosensor exhibited comparable sensitivity toward the CEA detection in comparison with other sensors (**Table S2**). Given the dosage of AgNCs@Apt@UiO-66 nanocomposite containing the CEA targeted aptamer strands, the SPR biosensor can be developed directly without the additional immobilization of the probe, thereby providing a new method for feasible and fast sensing of the analytes.

Kinetics analysis of the developed aptasensor. The adsorption behavior of CEA is consistent with the Langmuir isotherm, which can be described by the following equation:[57]

$$C_e/q = C_e/q_m + 1/(K \times q_m), \quad (1)$$

where q is the SPR signal of CEA adsorbed onto the AgNC@Apt@UiO-66-modifed Au surface when reaching equilibrium, q_m is the saturated adsorbed amount of CEA, C_e is the concentration of CEA in the bulk solution, and K reflects the affinity of the CEA toward adsorption sites. The plot of C_e/q versus concentration C_e exhibits a straight line with parameters K and q_m derived from the intercept and slope (**Figure S7a**). The regression equation is $C_e/q = 0.01247 + 4.2026\times10^{-4}C_e$ with a correlation coefficient R^2 of 0.994. The saturated adsorbed amount (q_m) of CEA is 2379.479 *RU*, and K is 0.0337 (ng·mL^{-1})$^{-1}$.

In the present study, parameter K, which reflects the affinity of the CEA toward

adsorption sites at 298 K, could be presented as follows:

$$K = \frac{1}{C_{solvent}} \exp\left(\frac{-\Delta G_{ads}}{RT}\right) \quad (2)$$

where R ($J \cdot mol^{-1} \cdot K^{-1}$) is the gas constant, T (K) is the temperature, ΔG ($kJ \cdot mol^{-1}$) is the free energy of adsorption, and $C_{solvent}$ is the molar concentration of a solvent, which is water ($C_{H2O} = 9.99 \times 10^8$ $ng \cdot mL^{-1}$) in this case. The ΔG of adsorption of CEA onto the AgNCs@Apt@UiO-66-modifed Au surface in phosphate buffer solution at 298 K is −42.94 $kJ \cdot mol^{-1}$, indicating the strong adsorption of CEA onto the AgNCs@Apt@UiO-66-modifed Au surface, which confirmed that the CEA could specifically combine with aptmer.[58] According to the similar simulation method, the affinity constants (K) and ΔG_{ads} of the CEA adsorption onto the AgNCs@Apt@UiO-66-based sensor were also obtained from the EIS and DPV measurements result (**Figure 3**). The related simulation descriptions are shown in **S6**, and the comparison of K obtained using different methods is summarized in **Table S3**. The lowest K was originated from the present SPR aptasensor based on AgNCs@Apt@UiO-66 nanocomposite. However, no substantial difference was observed among the ΔG_{ads} values of three methods, suggesting the strong affinity of AgNCs@Apt@UiO-66-based aptasensor.

Selectivity, reproducibility, and stability of the proposed aptasensor. The selectivity of the AgNCs@Apt@UiO-66-based electrochemical aptasensor was measured by examining the response of the proposed aptasensor to the other interferences, including AA, MUC1, thrombin, IgG, and their mixed solution, which possibly coexist with CEA. The concentration of the interferences (1.0 $ng \cdot mL^{-1}$) was

100 times of CEA (0.01 ng·mL^{-1}). The result for the selectivity assessment of CEA is illustrated in **Figure 6a**. In contrast to the significant response of the ΔR_{ct} values as observed for the detection of CEA and mixed solution containing CEA, negligible response variations were obtained with the addition of other interferences. Consequently, the result showed high selectivity of the electrochemical aptasensor for CEA over other interferences. It is due to the high specific recognition between CEA and its corresponding probe aptamer. For further exploiting the possible application of the fabricated aptasensor in clinical diagnoses and biological monitoring, the stability and reproducibility should be investigated. After AgNCs@Apt@UiO-66-based aptasensor was stored at 4 °C for 11 days, EIS was used to detect the electrochemical response in $[Fe(CN)_6]^{3-/4-}$ and 0.1 M PBS containing 0.01 ng·mL^{-1} CEA (**Figure 6b**). This result showed that no apparent change in response to 0.01 ng·mL^{-1} CEA was found after 9 days. Over the next two days, the ΔR_{ct} value increased by about 11.88%, and the relative standard deviation (RSD) was calculated to be 4.74%.

The reproducibility of the aptasensor was tested by detecting the ΔR_{ct} values caused by the addition of CEA (0.01 ng·mL^{-1}) in $[Fe(CN)_6]^{3-/4-}$ and 0.1 M PBS at room temperature (25 °C) with five AgNCs@Apt@UiO-66-based aptasensors, which were prepared under the same condition (**Figure 6c**). The ΔR_{ct} values of the five aptasensors for detecting CEA had a RSD of 2.75%. All of these suggest that the developed aptasensor not only exhibits acceptable stability but also possesses good sensor-to-sensor reproducibility. The regenerability of the fabricated aptasensor was evaluated by immersing the CEA-bound nanocomposite electrode into 1.0 M NaOH

at 4 ℃ for 5 min, followed by rinsing with a large amount of ultrapure water. Afterwards, the treated electrode was immersed into the CEA solution (0.01 ng·mL^{-1}). As shown in **Figure 6d**, no substantial change in R_{ct} values of the proposed aptasensor was observed during the first seven regeneration runs, indicating that the aptasensor could be facilely regenerated.

SPR measurements were also performed to investigate the selectivity, stability, reproducibility, and regenerability, as shown in **Figure S9**, **S10**, and **S11**, respectively. It demonstrated that the close results were obtained. All results revealed that the fabricated aptasensor exhibits good biosensing performance, such as high sensitivity, good selectivity, high stability, acceptable reproducibility, and good regenerability. Therefore, it confirmed that the resultant AgNCs@Apt@UiO-66 nanocomposite can be explored as the bifunctional aptasensor of electrochemical and SPR aptasensor, further broadening the application fields of MOF-based sensors.

Real sample analysis. To verify the applicability of the proposed sensing platform, the practical use of the developed electrochemical aptasensor for CEA detection in real sample was investigated by detecting CEA in human serum sample. Different CEA concentrations were spiked into the treated human serum sample, and the presence of CEA was detected and analyzed using the AgNCs@Apt@UiO-66-based aptasensor through the electrochemical sensing method mentioned above. Results were obtained according to the standard curve in **Figure 5b**. As shown in **Table S4**, the recovery of this aptasensor ranged from 97.6% to 106%, and the RSD was less than 5%. SPR measurements were also performed to investigate

the applicability, as shown in **Table S5**. The results showed that the recoveries of the aptasensor were ranged from 95.6% to 109.5%, whereas RSD was less than 5%. It suggested that this new strategy exhibits high reproducibility, accuracy, and feasibility for rapidly detecting CEA in human serum.

■CONCLUSIONS

A novel AgNCs@Apt@UiO-66 nanocomposite was prepared and explored as platform to construct the electrochemical and SPR aptasensors for detecting CEA simultaneously. The AgNCs@Apt@UiO-66-based aptasensor exhibited higher sensitivity toward CEA and adsorbed larger amount of CEA molecules than those of Apt@UiO-66-based aptasensor due to the combined advantages of Ag NCs, CEA aptamer, and UiO-66, including large specific surface area, good biocompatibility, strong bioaffinity, and high specificity. The low LODs obtained from the electrochemical techniques of EIS, DPV, and SPR, i.e., 8.88 $pg \cdot mL^{-1}$ (0.56 pM), 4.93 $pg \cdot mL^{-1}$ (0.31 pM), and 0.3 $ng \cdot mL^{-1}$ (18.8 pM), respectively, and good sensing performance provides a considerably promising approach for CEA detection. The affinity constant toward the CEA detection derived from SPR was lower than those of EIS and DPV, but they showed similar free energy of adsorption. All of these results revealed that the NC-embedded MOF nanomaterials not only can be explored as the electrochemical biosensor but also can be applied as the optical sensor. Thereby, the as-obtained AgNCs@Apt@UiO-66 nanocomposite can broaden potential applications in both biosensing and biomedical fields.

■ASSOCIATED CONTENT

Ⓢ Supporting Information

The Supporting Information is available free of charge on the ACS Publications website at DOI:

Chemicals and materials; pre-treatment of the bare Au electrode and the SPR chips; chemical structure, component of AgNCs@Apt@UiO-66; surface morphology; electrochemical performance of UiO-66 and AgNCs@Apt@UiO-66; Selectivity, stability, reproducibility and regenerability of the AgNCs@Apt@UiO-66-based SPR aptasensor; and real sample analysis (Word).

■AUTHOR INFORMATION

Corresponding Author

*E-mail: mainzhh@163.com.

ORCID

Zhihong Zhang: 0000-0002-5888-4107

Notes

The authors declare no competing financial interest.

■ACKNOWLEDGEMENTS

We are grateful to the support from the National Natural Science Foundation of China (NSFC: Account Nos. U1604127 and 21601161), and Innovative Technology Team of Henan Province (CXTD2014042).

REFERENCES

(1) Hasanzadeh, M., Shadjou, N., Lin, Y., de la Guardia, M., Nanomaterials for Use

in Immunosensing of Carcinoembryonic Antigen (CEA): Recent Advances. *TrAC-Trend. Anal. Chem.* **2017**, *86*, 185-205.

(2) Dong, J., Sun, G., Zhu, H., Diagnostic Value of Soluble Receptor-Binding Cancer Antigen Expressed on SiSo Cells and Carcinoembryonic Antigen in Differentiating Malignant From Benign Pleural Effusion. *Tumor Biol.* **2016**, *37* (3), 3257-3264.

(3) Pandey, B., Demchenko, A. V., Stine, K. J., Nanoporous Gold as a Solid Support for Protein Immobilization and Development of an Electrochemical Immunoassay for Prostate Specific Antigen and Carcinoembryonic Antigen. *Microchim. Acta* **2012**, *179* (1), 71-81.

(4) Liu, J., Wang, J., Wang, T., Li, D., Xi, F., Wang, J., Wang, E., Three-Dimensional Electrochemical Immunosensor for Sensitive Detection of Carcinoembryonic Antigen Based on Monolithic and Macroporous Graphene Foam. *Biosens. Bioelectron.* **2015**, *65*, 281-286.

(5) Chen, Z., Liang, R., Guo, X., Liang, J., Deng, Q., Li, M., An, T., Liu, T., Wu, Y., Simultaneous Quantitation of Cytokeratin-19 Fragment and Carcinoembryonic Antigen in Human Serum Via Quantum Dot-Doped Nanoparticles. *Biosens. Bioelectron.* **2017**, *91*, 60-65.

(6) Liu, Y., Yue, H., Tian, W., Chen, Y., Li, F., Quantification of Carcinoembryonic Antigen by Capillary Electrophoresis-Chemiluminescence Detection using Internal Standard Method. *Anal. Lett.* **2009**, *31* (7), vii - ix.

(7) Pang, X., Li, J., Zhao, Y., Wu, D., Zhang, Y., Du, B., Ma, H., Wei, Q.,

Label-Free Electrochemiluminescent Immunosensor for Detection of Carcinoembryonic Antigen Based on Nanocomposites of GO/MWCNTs-COOH/Au@CeO_2. *ACS Appl. Mater. Inter.* **2015**, *7* (34), 19260-19267.

(8) Feng, T., Qiao, X., Wang, H., Sun, Z., Hong, C., A Sandwich-Type Electrochemical Immunosensor for Carcinoembryonic Antigen Based on Signal Amplification Strategy of Optimized Ferrocene Functionalized Fe_3O_4@SiO_2 as Labels. *Biosens. Bioelectron.* **2016**, *79*, 48-54.

(9) Zeng, S., Baillargeat, D., Ho, H., Yong, K., Nanomaterials Enhanced Surface Plasmon Resonance for Biological and Chemical Sensing Applications. *Chem. Soc. Rev.* **2014**, *43* (10), 3426-3452.

(10) Park, J., Byun, J., Mun, H., Shim, W., Shin, Y., Li, T., Kim, M., A Regeneratable, Label-Free, Localized Surface Plasmon Resonance (LSPR) Aptasensor for the Detection of Ochratoxin a. *Biosens. Bioelectron.* **2014**, *59*, 321-327.

(11) Hu, W., He, G., Zhang, H., Wu, X., Li, J., Zhao, Z., Qiao, Y., Lu, Z., Liu, Y., Li, C. M., Polydopamine-Functionalization of Graphene Oxide to Enable Dual Signal Amplification for Sensitive Surface Plasmon Resonance Imaging Detection of Biomarker. *Anal. Chem.* **2014**, *86* (9), 4488-4493.

(12) Steinicke, F., Oltmann-Norden, I., Wätzig, H., Long Term Kinetic Measurements Revealing Precision and General Performance of Surface Plasmon Resonance Biosensors. *Anal. Biochem.* **2017**, *530*, 94-103.

(13) Špringer, T., Chadtová Song, X., Ermini, M. L., Lamačová, J., Homola, J.,

Functional Gold Nanoparticles for Optical Affinity Biosensing. *Anal. Bioanal. Chem.* **2017**, *409* (16), 4087-4097.

(14) Willner, I., Zayats, M., Electronic Aptamer-Based Sensors. *Angew. Chem. Int. Edit.* **2007**, *46* (34), 6408-6418.

(15) Wu, Y., Wang, A., Ding, X., Xu, F., Versatile Functionalization of Poly(Methacrylic acid) Brushes with Series of Proteolytically Cleavable Peptides for Highly Sensitive Protease Assay. *ACS Appl. Mater. Inter.* **2017**, *9* (1), 127-135.

(16) Wu, Y., Nizam, M. N., Ding, X., Xu, F., Rational Design of Peptide-Functionalized Poly(Methacrylic Acid) Brushes for On-Chip Detection of Protease Biomarkers. *ACS Biomater. Sci. & Eng.* **2017**, 10.1021/acsbiomaterials.7b00584.

(17) Zhang, Z., Ji, H., Song, Y., Zhang, S., Wang, M., Jia, C., Tian, J., He, L., Zhang, X., Liu, C., Fe(III)-based Metal-Organic Framework-Derived Core-Shell Nanostructure: Sensitive Electrochemical Platform for High Trace Determination of Heavy Metal Ions. *Biosens. Bioelectron.* **2017**, *94*, 358-364.

(18) Fang, S., Dong, X., Liu, S., Penng, D., He, L., Wang, M., Fu, G., Feng, X., Zhang, Z., A Label-Free Multi-Functionalized Electrochemical Aptasensor Based on a Fe_3O_4@3D-rGO@Plasma-Polymerized (4-Vinyl Pyridine) Nanocomposite for the Sensitive Detection of Proteins in Whole Blood. *Electrochim. Acta* **2016**, *212*, 1-9.

(19) Hashkavayi, A. B., Raoof, J. B., Ojani, R., Kavoosian, S., Ultrasensitive Electrochemical Aptasensor Based on Sandwich Architecture for Selective Label-Free Detection of Colorectal Cancer (CT26) Cells. *Biosens. Bioelectron.* **2017**, *92*,

630-637.

(20) Khang, H., Cho, K., Chong, S., Lee, J. H., All-In-One Dual-Aptasensor Capable of Rapidly Quantifying Carcinoembryonic Antigen. *Biosens. Bioelectron.* **2017**, *90*, 46-52.

(21) Ahn, J. K., Kim, H. Y., Baek, S., Park, H. G., A New S-Adenosylhomocysteine Hydrolase-Linked Method for Adenosine Detection Based on DNA-templated Fluorescent Cu/Ag Nanoclusters. *Biosens. Bioelectron.* **2017**, *93*, 330-334.

(22) Zhang, L., Liang, R., Xiao, S., Bai, J., Zheng, L., Zhan, L., Zhao, X., Qiu, J., Huang, C., DNA-templated Ag Nanoclusters as Fluorescent Probes for Sensing and Intracellular Imaging of Hydroxyl Radicals. *Talanta* **2014**, *118*, 339-347.

(23) Yang, H., Wang, Y., Chen, X., Zhao, X., Gu, L., Huang, H., Yan, J., Xu, C., Li, G., Wu, J., Edwards, A. J., Dittrich, B., Tang, Z., Wang, D., Lehtovaara, L., Häkkinen, H., Zheng, N., Plasmonic Twinned Silver Nanoparticles with Molecular Precision. *Nat. Commun.* **2016**, *7*, 12809.

(24) Paul, D., Dutta, S., Saha, D., Biswas, R., LSPR Based Ultra-sensitive Low Cost U-bent Optical Fiber for Volatile Liquid Sensing. *Sensor. Actuat. B-Chem.* **2017**, *250*, 198-207.

(25) Majumdar, D., Singha, A., Mondal, P. K., Kundu, S., DNA-Mediated Wirelike Clusters of Silver Nanoparticles: An Ultrasensitive SERS Substrate. *ACS Appl. Mater. Inter.* **2013**, *5* (16), 7798-7807.

(26) Lee, S., Kapustin, E. A., Yaghi, O. M., Coordinative Alignment of Molecules in Chiral Metal-Organic Frameworks. *Science* **2016**, *353* (6301), 808.

(27) Bhakta, R. K., Herberg, J. L., Jacobs, B., Highley, A., Behrens, R., Ockwig, N. W., Greathouse, J. A., Allendorf, M. D., Metal-Organic Frameworks as Templates for Nanoscale $NaAlH_4$. *J. Am. Chem. Soc.* **2009**, *131* (37), 13198-13199.

(28) Pramudya, Y., Mendoza-Cortes, J. L., Design Principles for High H_2 Storage Using Chelation of Abundant Transition Metals in Covalent Organic Frameworks for 0 – 700 Bar at 298 K. *J. Am. Chem. Soc.* **2016**, *138* (46), 15204-15213.

(29) Wuttke, S., Lismont, M., Escudero, A., Rungtaweevoranit, B., Parak, W. J., Positioning Metal-Organic Framework Nanoparticles within the Context of Drug delivery-A Comparison with Mesoporous Silica Nanoparticles and Dendrimers. *Biomaterials* **2017**, *123*, 172-183.

(30) Jin, M., Mou, Z., Zhang, R., Liang, S., Zhang, Z., An Efficient Ratiometric Fluorescence Sensor Based on Metal-Organic Frameworks and Quantum Dots for Highly Selective Detection of 6-Mercaptopurine. *Biosens. Bioelectron.* **2017**, *91*, 162-168.

(31) Zheng, L., Li, X., Du, W., Shi, D., Ning, W., Lu, X., Hou, Z., Metal-Organic Framework Derived Cu/ZnO Catalysts for Continuous Hydrogenolysis of Glycerol. *Appl. Catal. B-Environ.* **2017**, *203*, 146-153.

(32) He, C., Lu, K., Liu, D., Lin, W., Nanoscale Metal-Organic Frameworks for the Co-Delivery of Cisplatin and Pooled siRNAs to Enhance Therapeutic Efficacy in Drug-Resistant Ovarian Cancer Cells. *J. Am. Chem. Soc.* **2014**, *136* (14), 5181-5184.

(33) Chen, M., Gan, N., Zhou, Y., Li, T., Xu, Q., Cao, Y., Chen, Y., A Novel Aptamer-Metal Ions- Nanoscale MOF Based Electrochemical Biocodes for Multiple

Antibiotics Detection and Signal Amplification. *Sensor. Actuat. B-Chem.* **2017**, *242*, 1201-1209.

(34) Zhang, G., Zhuang, Y., Shan, D., Su, G., Cosnier, S., Zhang, X., Zirconium-Based Porphyrinic Metal-Organic Framework (PCN-222): Enhanced Photoelectrochemical Response and its Application for Label-Free Phosphoprotein Detection. *Anal. Chem.* **2016**, *88* (22), 11207-11212.

(35) Zhao, H., Qiu, G., Liang, Z., Li, M., Sun, B., Qin, L., Yang, S., Chen, W., Chen, J., A zinc(II)-based Two-Dimensional MOF for Sensitive and Selective Sensing of HIV-1 ds-DNA Sequences. *Anal. Chim. Acta* **2016**, *922*, 55-63.

(36) Zhang, C., Wang, X., Hou, M., Li, X., Wu, X., Ge, J., Immobilization on Metal-Organic Framework Engenders High Sensitivity for Enzymatic Electrochemical Detection. *ACS Appl. Mater. Inter.* **2017**, *9* (16), 13831-13836.

(37) Liu, C., Sun, C., Tian, J., Wang, Z., Ji, H., Song, Y., Zhang, S., Zhang, Z., He, L., Du, M., Highly Stable Aluminum-Based Metal-Organic Frameworks as Biosensing Platforms for Assessment of Food Safety. *Biosens. Bioelectron.* **2017**, *91*, 804-810.

(38) Cavka, J. H., Jakobsen, S., Olsbye, U., Guillou, N., Lamberti, C., Bordiga, S., Lillerud, K. P., A New Zirconium Inorganic Building Brick Forming Metal Organic Frameworks with Exceptional Stability. *J. Am. Chem. Soc.* **2008**, *130* (42), 13850-13851.

(39) Zhu, X., Gu, J., Wang, Y., Li, B., Li, Y., Zhao, W., Shi, J., Inherent Anchorages in UiO-66 Nanoparticles for Efficient Capture of Alendronate and its Mediated Release. *Chem. Commun.* **2014**, *50* (63), 8779-8782.

(40) Liu, C., Zhang, Z., Chen, M., Zhao, H., Duan, F., Chen, D., Wang, M., Zhang, S., Du, M., Pore Modulation of Zirconium-Organic Frameworks for High-Efficiency Detection of Trace Proteins. *Chem. Commun.* **2017**, *53* (28), 3941-3944.

(41) Zhang, G., Cai, C., Cosnier, S., Zeng, H., Zhang, X., Shan, D., Zirconium-Metalloporphyrin Frameworks as a Three-In-One Platform Possessing Oxygen Nanocage, Electron Media, and Bonding Site for Electrochemiluminescence Protein Kinase Activity Assay. *Nanoscale* **2016**, *8* (22), 11649-11657.

(42) Campbell, C. T., Kim, G., SPR Microscopy and its Applications to High-Throughput Analyses of Biomolecular Binding Events and their Kinetics. *Biomaterials* **2007**, *28* (15), 2380-2392.

(43) He, L., Duan, F., Song, Y., Guo, C., Zhao, H., Tian, J., Zhang, Z., Liu, C., Zhang, X., Wang, P., Du, M., Fang, S., 2D Zirconium-Based Metal-Organic Framework Nanosheets for Highly Sensitive Detection of Mucin 1: Consistency Between Electrochemical and Surface Plasmon Resonance Methods. *2D Materials* **2017**, *4* (2), 025098.

(44) Liu, L., Song, Y., Chong, H., Yang, S., Xiang, J., Jin, S., Kang, X., Zhang, J., Yu, H., Zhu, M., Size-Confined Growth of Atom-Precise Nanoclusters in Metal-Organic Frameworks and their Catalytic Applications. *Nanoscale* **2016**, *8* (3), 1407-1412.

(45) Luan, J., Hu, R., Tadepalli, S., Morrissey, J. J., Kharasch, E. D., Singamaneni, S., Amplification of Refractometric Biosensor Response through Biomineralization of Metal-Organic Framework Nanocrystals. *Adv. Mater. Technol.* **2017**, *2* (7), 1700023.

(46) Wang, W., Wang, L., Zou, L., Li, G., Ye, B., Electrochemical Behavior of

Arctigenin at a Novel Voltammetric Sensor Based on Iodide/SWCNTs Composite Film Modified Electrode and its Sensitive Determination. *J. Electroanal. Chem.* **2016**, *772* (Supplement C), 17-26.

(47) Stenberg, E., Persson, B., Roos, H., Urbaniczky, C., Quantitative Determination of Surface Concentration of Protein with Surface Plasmon Resonance Using Radiolabeled Proteins. *J. Colloid Interf. Sci.* **1991**, *143* (2), 513-526.

(48) Wu, Z., Li, H., Liu, Z., An Aptasensor for Carcinoembryonic Antigen Based on Upconversion Fluorescence Resonance Energy Transfer. *Sensor. Actuat. B-Chem.* **2015**, *206*, 531-537.

(49) Fang, S., Dong, X., Ji, H., Liu, S., Yan, F., Peng, D., He, L., Wang, M., Zhang, Z., Electrochemical Aptasensor for Lysozyme Based on a Gold Electrode Modified with a Nanocomposite Consisting of Reduced Graphene Oxide, Cuprous Oxide, and Plasma-Polymerized Propargylamine. *Microchim. Acta* **2016**, *183* (2), 633-642.

(50) Devi, T. B., Ahmaruzzaman, M., Bio-Inspired Facile and Green Fabrication of Au@Ag@AgCl Core-Double Shells Nanoparticles and their Potential Applications for Elimination of Toxic Emerging Pollutants: A Green and Efficient Approach for Wastewater Treatment. *Chem. Eng. J.* **2017**, *317*, 726-741.

(51) Kulkarni, A. A., Bhanage, B. M., Ag@AgCl Nanomaterial Synthesis Using Sugar Cane Juice and its Application in Degradation of Azo Dyes. *ACS Sustain. Chem. Eng.* **2014**, *2* (4), 1007-1013.

(52) Top, M., Er, O., Congur, G., Erdem, A., Lambrecht, F. Y., Intracellular Uptake Study of Radiolabeled Anticancer Drug and Impedimetric Detection of its Interaction

with DNA. *Talanta* **2016**, *160*, 157-163.

(53) Flanagan, M. T., Hesketh, T. R., Electrostatic Interactions in the Binding of Fluorescent Probes to Lipid Membranes. *BBA-Biomembranes* **1973**, *298* (3), 535-545.

(54) Ravi Kumar, M. N. V., Bakowsky, U., Lehr, C. M., Preparation and Characterization of Cationic PLGA Nanospheres as DNA Carriers. *Biomaterials* **2004**, *25* (10), 1771-1777.

(55) Meng, H., Fu, T., Zhang, X., Wang, N., Tan, W., Shen, G., Yu, R., Efficient Fluorescence Turn-On Probe for Zirconium via a Target-Triggered DNA Molecular Beacon Strategy. *Anal. Chem.* **2012**, *84* (5), 2124-2128.

(56) Zhang, G., Zhuang, Y., Shan, D., Su, G., Cosnier, S., Zhang, X., Zirconium-Based Porphyrinic Metal‐Organic Framework (PCN-222): Enhanced Photoelectrochemical Response and its Application for Label-Free Phosphoprotein Detection. *Anal. Chem.* **2016**, *88* (22), 11207-11212.

(57) Muzic, M., Sertic-Bionda, K., Gomzi, Z., Kinetic and Statistical Studies of Adsorptive Desulfurization of Diesel Fuel on Commercial Activated Carbons. *Chem. Eng. Technol.* **2008**, *31* (3), 355-364.

(58) Cheng, X., Roscoe, S. G., Corrosion Behavior of Titanium in the Presence of Calcium Phosphate and Serum Proteins. *Biomaterials* **2005**, *26* (35), 7350-7356.

(59) Lu, W., Wang, K., Xiao, K., Qin, W., Hou, Y., Xu, H., Yan, X., Chen, Y., Cui, D., He, J., Dual Immunomagnetic Nanobeads-Based Lateral Flow Test Strip for Simultaneous Quantitative Detection of Carcinoembryonic Antigen and Neuron Specific Enolase. *Sci. Rep.-UK* **2017**, *7*, 42414.

(60) Yang, T., Gao, Y., Liu, Z., Xu, J., Lu, L., Yu, Y., Three-Dimensional Gold Nanoparticles/Prussian Blue-Poly(3,4-Ethylenedioxythiophene) Nanocomposite as Novel Redox Matrix for Label-Free Electrochemical Immunoassay of Carcinoembryonic Antigen. *Sensor. Actuat. B-Chem.* **2017**, *239*, 76-84.

(61) Zhao, L., Li, C., Qi, H., Gao, Q., Zhang, C., Electrochemical Lectin-Based Biosensor Array for Detection and Discrimination of Carcinoembryonic Antigen Using Dual Amplification of Gold Nanoparticles and Horseradish Peroxidase. *Sensor. Actuat. B-Chem.* **2016**, *235*, 575-582.

(62) Zhu, J., Wang, J., Li, J., Zhao, J., Specific Detection of Carcinoembryonic Antigen Based on Fluorescence Quenching of Au-Ag Core-Shell Nanotriangle Probe. *Sensor. Actuat. B-Chem.* **2016**, *233*, 214-222.

Figure captions

Figure 1. Schematic diagram of the AgNCs@Apt@UiO-66-based aptasensor for detecting CEA, including (i) preparation of UiO-66, (ii) preparation of AgNCs@Apt@UiO-66, and (iii) detection of CEA.

Figure 2. Ag 3*d* and P 2*p* core-level XPS spectra of (a) AgNCs@Apt@UiO-66 and (b) CEA/AgNCs@Apt@UiO-66 nanocomposites.

Figure 3. (a, b) Low- and high-magnitude SEM and (c, d) HR-TEM images of AgNCs@Apt@UiO-66 nanocomposite, inset: the corresponding SAED.

Figure 4. (a, b) EIS plots and (c, d) DPV curves to trace the whole procedure of the CEA detection using the developed aptasensor based on (a, c) AgNCs@Apt@UiO-66 and (b, d) UiO-66, respectively, in $[Fe(CN)_6]^{3-/4-}$ (5 mM) and PBS (0.1 M). (e) Variation in the *RU* of (i) Apt/UiO-66/Au and (ii) AgNCs@Apt@UiO-66/Au for 10 $ng{\cdot}mL^{-1}$ of CEA solution.

Figure 5. (a) EIS responses and (c) DPV curves of the AgNCs@Apt@UiO-66/AE with different CEA concentrations (0, 0.01, 0.05, 0.1, 0.5, 1, 5, and 10 $ng{\cdot}mL^{-1}$). Dependence of (b) ΔR_{ct} and (d) ΔI_p on the concentration of CEA. The linear parts of the calibration curves are shown in the inset of (b) and (d). (e) SPR sensor responses of the AgNCs@Apt@UiO-66/Au with different CEA concentrations: (i) 1.0, (ii) 4.0, (iii) 5.0, (iv) 10.0, (v) 50, (vi) 100, and (vii) 250 $ng{\cdot}mL^{-1}$. (f) Dependence of the ΔRU of the modified Au surface on the concentration of CEA. The linear part of the calibration curve is shown in the inset of (f).

Figure 6. (a) ΔR_{ct} values of AgNCs@Apt@UiO-66-based electrochemical aptasensor

by separately adding the interferences (AA, MUC1, thrombin, and IgG with the concentration of 1.0 ng·mL^{-1}), CEA (0.01 ng·mL^{-1}), and their mixture. (b) Stability of the AgNCs@Apt@UiO-66-based electrochemical aptasensor for detecting CEA (0.01 ng·mL^{-1}) within 15 days. (c) Reproducibility and (d) regenerability of the AgNCs@Apt@UiO-66-based aptasensor for detecting CEA with the concentration of 0.01 ng·mL^{-1}.

Figures

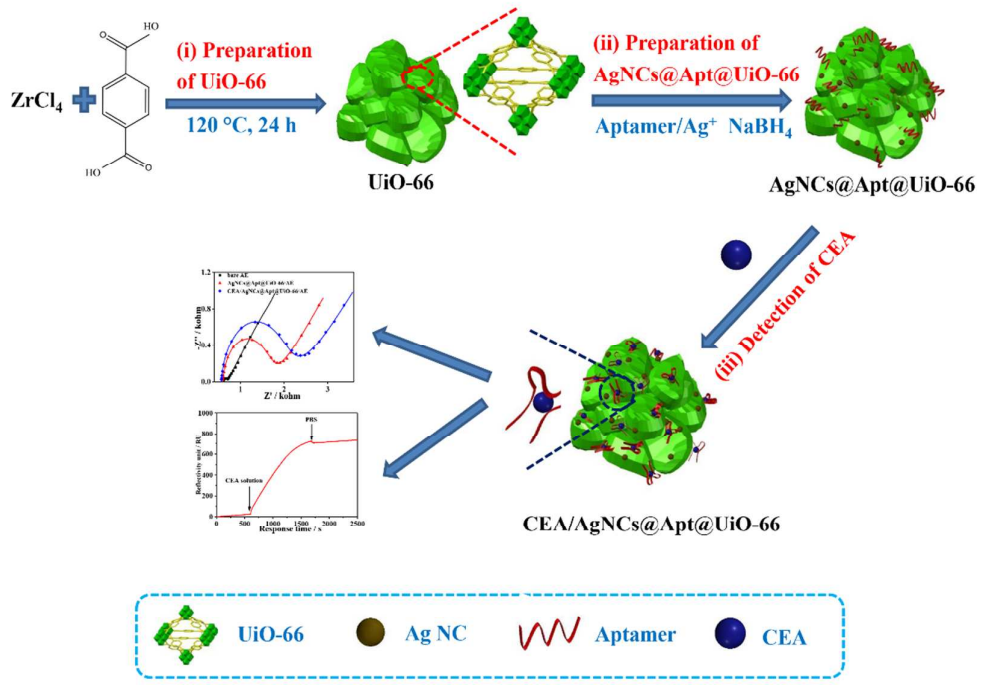

Figure 1

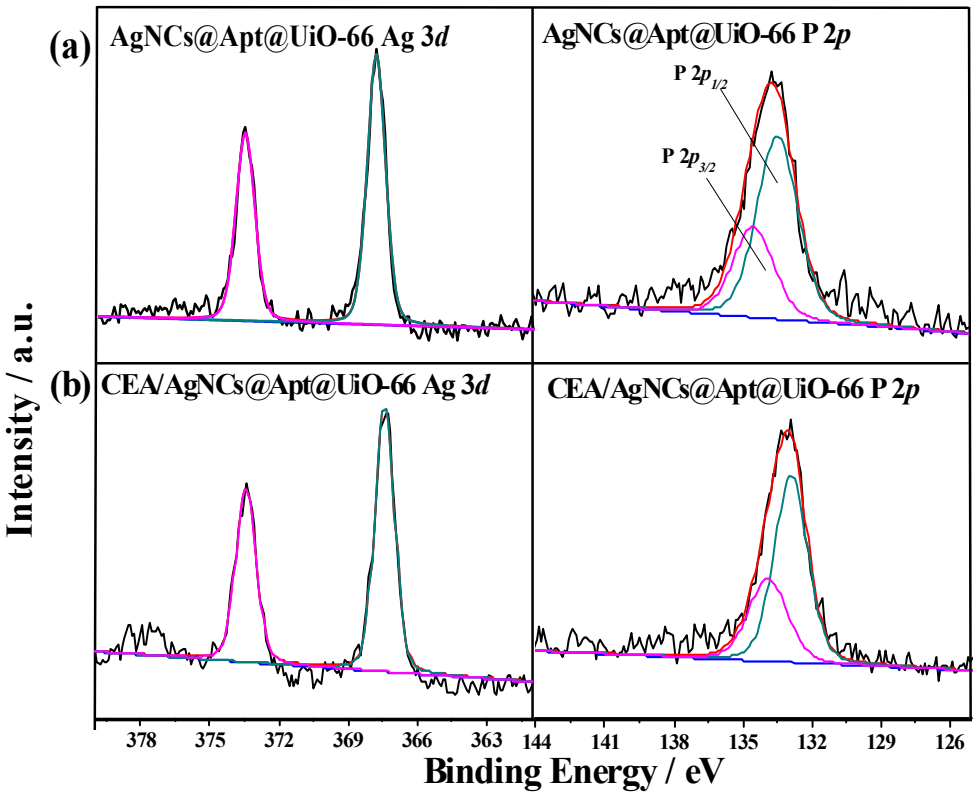
(a)
AgNCs@Apt@UiO-66 Ag 3d
AgNCs@Apt@UiO-66 P 2p
P 2p1/2
P 2p3/2
(b)
CEA/AgNCs@Apt@UiO-66 Ag 3d
CEA/AgNCs@Apt@UiO-66 P 2p
Intensity / a.u.
378 375 372 369 366 363 144 141 138 135 132 129 126
Binding Energy / eV

Figure 2

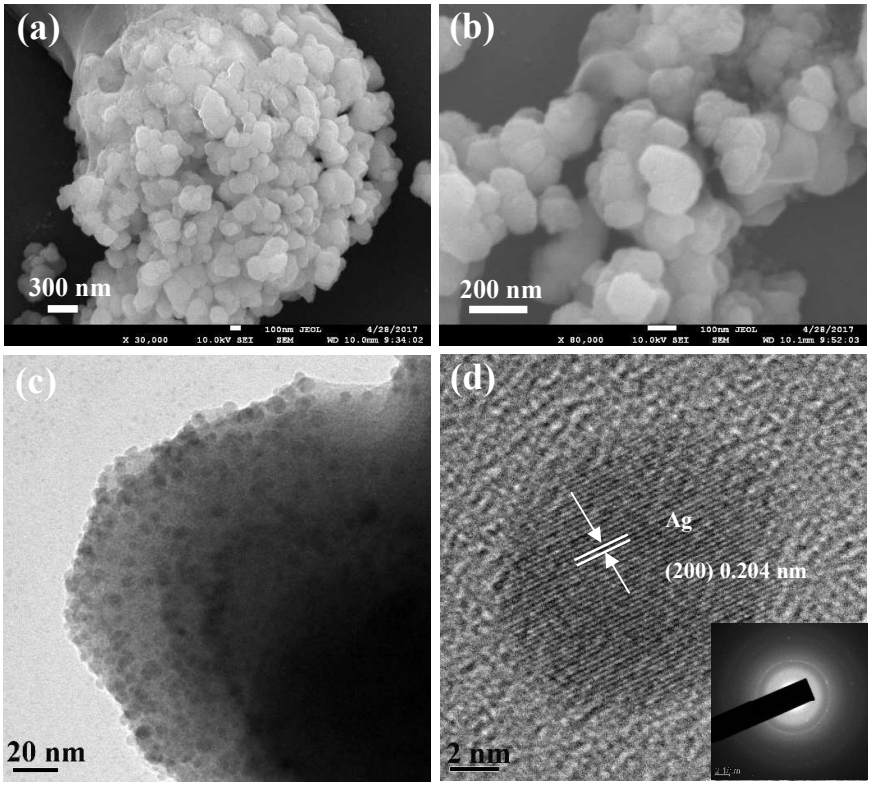

Figure 3

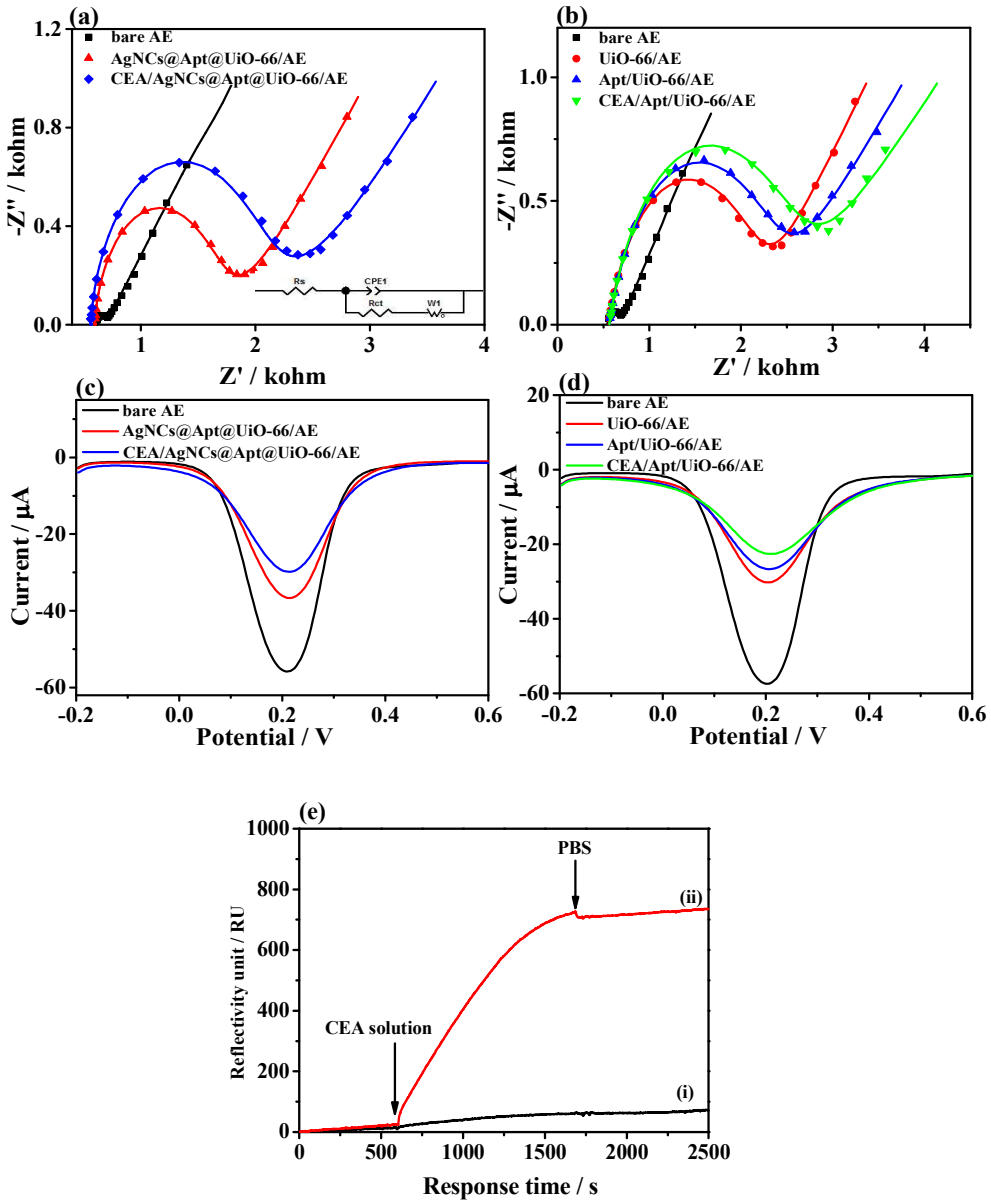
(a)
bare AE
AgNCs@Apt@UiO-66/AE
CEA/AgNCs@Apt@UiO-66/AE
-Z'' / kohm
Z' / kohm
Rs
CPE1
Rct
W1
(b)
bare AE
UiO-66/AE
Apt/UiO-66/AE
CEA/Apt/UiO-66/AE
-Z'' / kohm
Z' / kohm
(c)
bare AE
AgNCs@Apt@UiO-66/AE
CEA/AgNCs@Apt@UiO-66/AE
Current / μA
Potential / V
(d)
bare AE
UiO-66/AE
Apt/UiO-66/AE
CEA/Apt/UiO-66/AE
Current / μA
Potential / V
(e)
PBS
(ii)
CEA solution
(i)
Reflectivity unit / RU
Response time / s

Figure 4

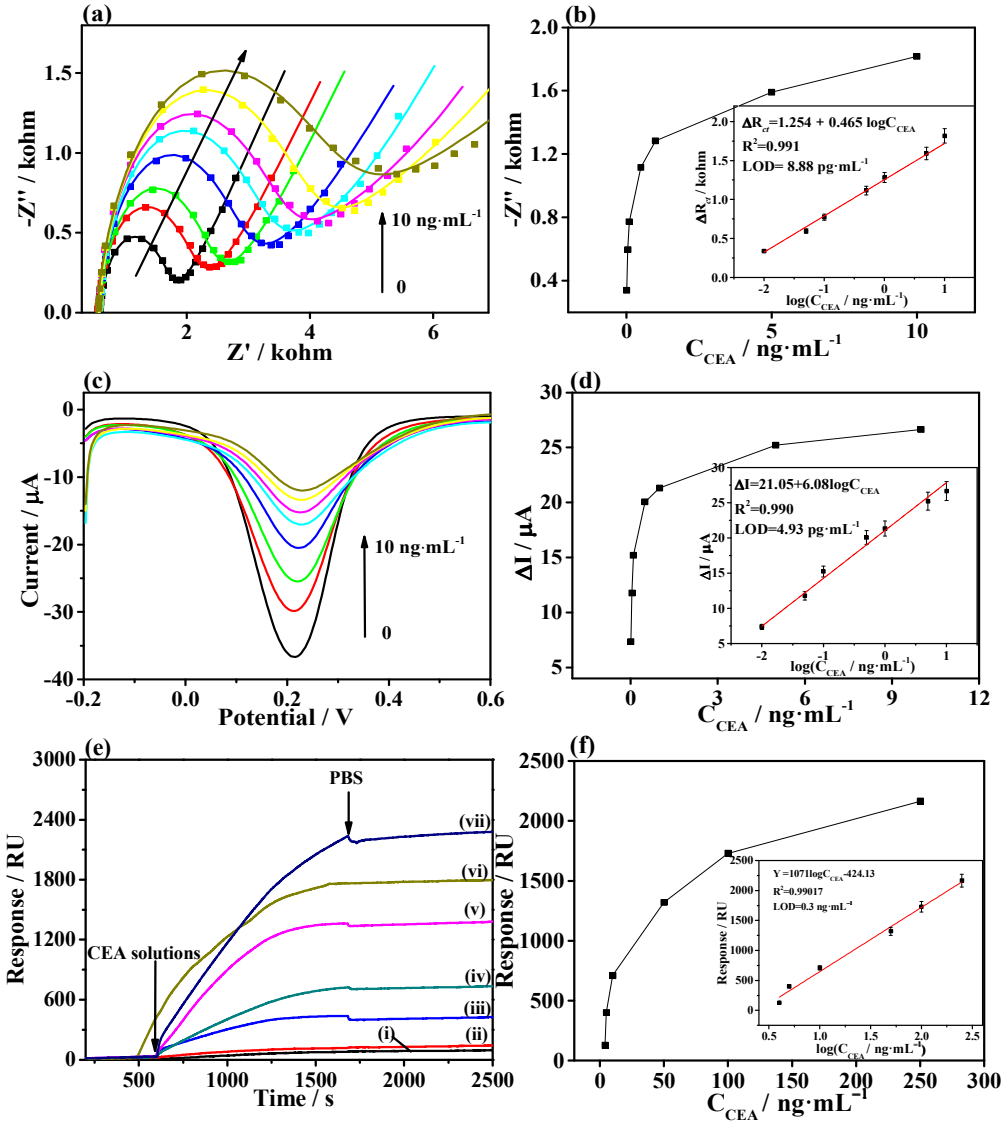
(a)
-Z'' / kohm
Z' / kohm
10 ng·mL-1
0
(b)
-Z'' / kohm
ΔRct=1.254 + 0.465 logCCEA
R2=0.991
LOD= 8.88 pg·mL-1
ΔRct / kohm
log(CCEA / ng·mL-1)
CCEA / ng·mL-1
(c)
Current / μA
Potential / V
10 ng·mL-1
0
(d)
ΔI / μA
ΔI=21.05+6.08logCCEA
R2=0.990
LOD=4.93 pg·mL-1
ΔI / μA
log(CCEA / ng·mL-1)
CCEA / ng·mL-1
(e)
Response / RU
Time / s
PBS
CEA solutions
(vii)
(vi)
(v)
(iv)
(iii)
(ii)
(i)
(f)
Response / RU
Y =1071logCCEA+424.13
R2=0.99017
LOD=0.3 ng·mL-1
Response / RU
log(CCEA / ng·mL-1)
CCEA / ng·mL-1

Figure 5

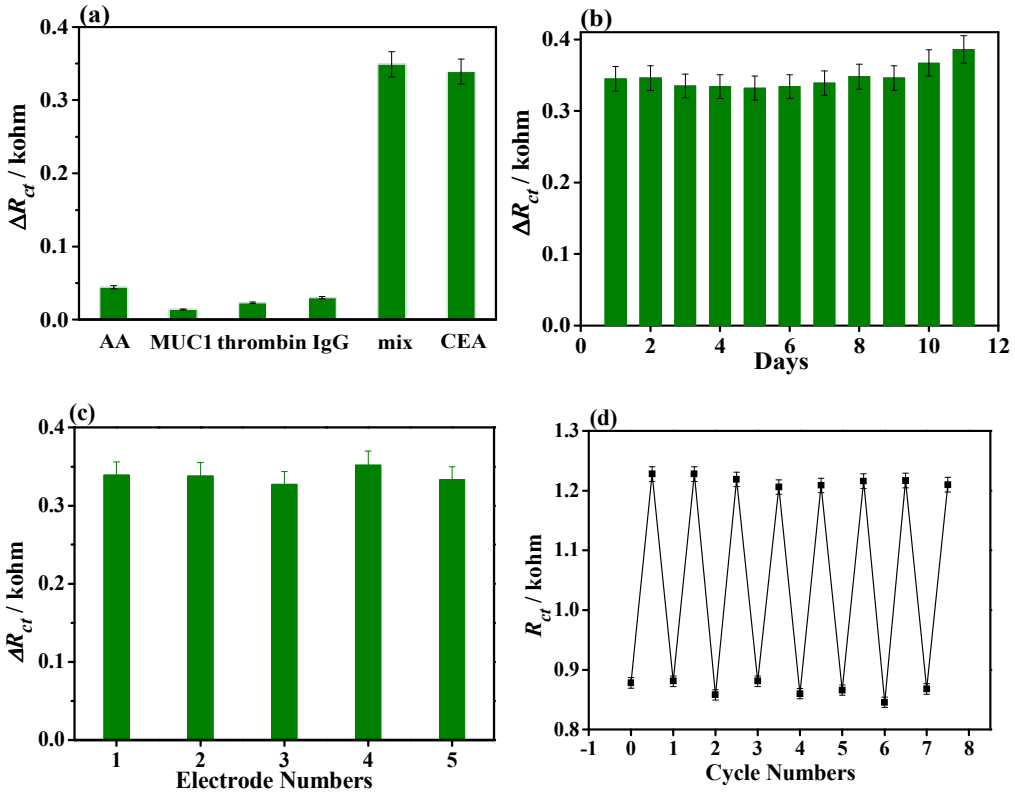
(a)
ΔR_{ct} / kohm
0.0
0.1
0.2
0.3
0.4
AA
MUC1
thrombin
IgG
mix
CEA
(b)
ΔR_{ct} / kohm
0.0
0.1
0.2
0.3
0.4
0
2
4
6
8
10
12
Days
(c)
ΔR_{ct} / kohm
0.0
0.1
0.2
0.3
0.4
1
2
3
4
5
Electrode Numbers
(d)
R_{ct} / kohm
0.8
0.9
1.0
1.1
1.2
1.3
-1
0
1
2
3
4
5
6
7
8
Cycle Numbers

Figure 6

Table

Table 1 Comparisons of the proposed approach with other electrochemical techniques for the detection of CEA.

Materials	**Detection method**	**Detection range** ($ng \cdot mL^{-1}$)	**LOD** ($pg \cdot mL^{-1}$)	**Ref.**
GO/MWCNTs-COOH/ Au@CeO_2	ECL	0.05−100	20	7
QD-doped polystyrene nanoparticles	fluorescence	2.8−680	350	5
All-in-one dual-aptasensor	chemiluminescence	3−200	580	20
Carboxyl-modified magnetic nanobeads	magnetic lateral flow test strip	1−50	45	59
AuNPs/PB-poly(3,4-ethylenedioxythiophene)	immunoassay	0.05−40	10	60
Electrochemical lectin-based biosensor	chronoamperometry	1−10	10	61
Silver coated-gold triangular nanoplates	fluorescence quenching	0.02−0.20	10	62
AgNCs@Apt@UiO-66	EIS	0.01−10	8.88	**This work**
	DPV	0.01−10	4.93	

TOC

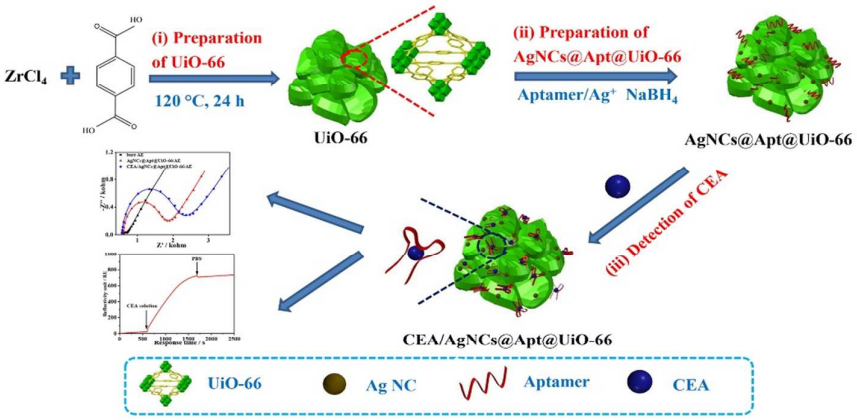
ZrCl4
(i) Preparation of UiO-66
120 °C, 24 h
UiO-66
(ii) Preparation of AgNCs@Apt@UiO-66
Aptamer/Ag+ NaBH4
AgNCs@Apt@UiO-66
(iii) Detection of CEA
CEA/AgNCs@Apt@UiO-66
UiO-66
Ag NC
Aptamer
CEA